12-1-2015

Large-Eddy Simulation of The Transient and Near-Equilibrium Behavior of Precipitating Shallow Convection

Axel Seifert
Deutscher Wetterdienst, axel.seifert@dwd.de

Thijs Heus
Cleveland State University, t.heus@csuohio.edu

Robert Pincus
University of Colorado

Bjorn Stevens
Max Planck Institute for Meteorology

RESEARCH ARTICLE

Large-eddy simulation of the transient and near-equilibrium behavior of precipitating shallow convection

Axel Seifert[1], Thijs Heus[2], Robert Pincus[3], and Bjorn Stevens[4]

[1]Hans-Ertel Centre for Weather Research, Deutscher Wetterdienst, Hamburg, Germany, [2]Department of Physics, Cleveland State University, Cleveland, Ohio, USA, [3]University of Colorado, and NOAA/Earth System Research Laboratory, Boulder, Colorado, USA, [4]Max Planck Institute for Meteorology, Hamburg, Germany

Abstract Large-eddy simulation is used to study the sensitivity of trade wind cumulus clouds to perturbations in cloud droplet number concentrations. We find that the trade wind cumulus system approaches a radiative-convective equilibrium state, modified by net warming and drying from imposed large-scale advective forcing. The system requires several days to reach equilibrium when cooling rates are specified but much less time, and with less sensitivity to cloud droplet number density, when radiation depends realistically on the vertical distribution of water vapor. The transient behavior and the properties of the near-equilibrium cloud field depend on the microphysical state and therefore on the cloud droplet number density, here taken as a proxy for the ambient aerosol. The primary response of the cloud field to changes in the cloud droplet number density is deepening of the cloud layer. This deepening leads to a decrease in relative humidity and a faster evaporation of small clouds and cloud remnants constituting a negative lifetime effect. In the near-equilibrium regime, the decrease in cloud cover compensates much of the Twomey effect, i.e., the brightening of the clouds, and the overall aerosol effect on the albedo of the organized precipitating cumulus cloud field is small.

1. Introduction

In Earth's atmosphere, cloud droplets form on cloud condensation nuclei (CCN). These CCN constitute part of the atmospheric aerosol. Anthropogenic activity has been shown to lead to an increase in aerosol particle concentrations and to an increase in the number of particles that can serve as CCN. An important question that has occupied cloud physicists since the mid 1970s has been if and how this increase in the number of CCN changes the properties of clouds and maybe even climate. *Twomey* [1977] demonstrated that because a higher number density of CCN will lead to higher cloud droplet number densities, cloud droplets will on average be smaller. This result follows from the assumption that the liquid water content of the cloud does not depend on the number of CCN because it is controlled by thermodynamic processes that depend on cloud macrostructure. Smaller cloud droplets mean that for a given amount of liquid water the available surface area to interact with radiation increases, thereby reflecting more sunlight and reducing its availability to be absorbed at the surface, or within the atmosphere. These ideas are strongly linked to a basic understanding of radiative transfer and there is ample evidence of aerosol perturbations causing a brightening of clouds, whether it be in laboratory environments, or in anthropogenic (ship tracks) or natural (volcanic) aerosol plumes.

It has also been conjectured that changes in CCN might influence cloud macrostructure. Most prominently, *Albrecht* [1989] argued that processes which reduce the average size of cloud droplets would retard and reduce the rain formation in clouds, resulting in longer-lived clouds. Longer living clouds would increase cloud cover and reflect even more sunlight, further cooling the atmosphere and surface. This type of aerosol-cloud interaction is often called a lifetime effect. Like the Twomey effect, the idea that smaller particles will form rain less readily is based on sound physical principles.

Given this strong foundation, it is somewhat surprising that empirical evidence for aerosol impacts on cloud macrophysics is so thin. Twenty-five years after *Albrecht*'s paper, the observational evidence for a lifetime effect in the marine cloud regimes for which it was postulated is limited and contradictory. *Boucher et al.* [2013] who assess the current level of our understanding, identify only one study, by *Yuan et al.* [2011],

Figure 1. Image of a simulated cloud field based on a ray tracing calculation at a wave length of 550 nm using a 3-D Monte Carlo radiation code of *Mayer* [2009]. Shown is simulation 15 of Table 1 after 40 h (by courtesy of Tobias Zinner of LMU Munich).

which provides observational evidence consistent with a lifetime effect. In that study a natural experiment, outgassing of SO_2 by the Kilauea volcano is used to study the effect of a changing aerosol environment on cloud macrophysical processes. But even in this case, the interpretation of the results are not without ambiguity, as precipitation affects both the outgassing aerosol precursors and their lifetime. Observational studies of ship tracks provide another inadvertent experiment within which one could hope to identify lifetime effects [*Conover*, 1969; *Durkee et al.*, 2000; *Hobbs et al.*, 2000], but in many cases the opposite response of clouds to aerosol perturbations is observed: some observations [*Christensen and Stephens*, 2011; *Chen et al.*, 2012] are consistent with more efficient mixing of smaller cloud drops leading to more rapid cloud desiccation and shorter lifetimes. Given the lack of observational evidence for a robust lifetime effect, it seems fair to question the viability of the underlying hypothesis.

Shallow maritime cumulus clouds are often thought of as a canonical cloud regime for expressing aerosol effects because they are often near a precipitation threshold and hence potentially sensitive to aerosol-cloud interactions. It was not by chance that *Albrecht* [1989] considered this regime when presenting his ideas. But focusing exclusively on direct links between cloud droplet number, precipitation rate, and cloud amount, ignores the rich suite of interactions and circulations that take place on scales between the microphysical scale on which CCN affect droplet concentrations and the macrophysical scales on which cloudiness evolves and albedo is primarily determined. In particular, it is becoming increasingly well appreciated that precipitation has a strong tendency to influence the organization of cloud fields, introducing a role for mesoscale processes which might alter direct links between macrophysical structure of cloud fields (e.g., their liquid water path, cloud cover, and albedo) and the microphysical changes within an updraft in an individual cloud. Organization of fields of shallow cumulus cloud fields over the ocean has long been observed [e.g., *Malkus and Riehl*, 1964; *Nair et al.*, 1998, among many others]; with the advent of very large domains it is also seen to emerge in large-eddy simulations of shallow marine cloudiness [see *Seifert and Heus*, 2013, and Figures 1 and 2].

This study addresses the question as to how cloud ensembles respond to aerosol perturbations when feedbacks include changes to local and mesoscale circulations. We do so by altering cloud droplet number density N as a proxy for the aerosol impact on clouds and quantifying the response of a field of clouds simulated within large domains, within which mesoscale circulations are free to emerge and organize the cloud systems. By using large-eddy simulation (LES) as an abstraction, we can investigate how changes in albedo, through possible changes in the propensity of clouds to precipitate, are influenced by the presence of organization.

2. Model Description and Setup

The University of California, Los Angeles large-eddy simulation (UCLA-LES) model of *Stevens et al.* [1999, 2005] is used here to simulate the cloud-topped boundary layer of marine subtropical subsidence regions, the trade wind regime. The UCLA-LES solves the anelastic equations and models the effect of unresolved
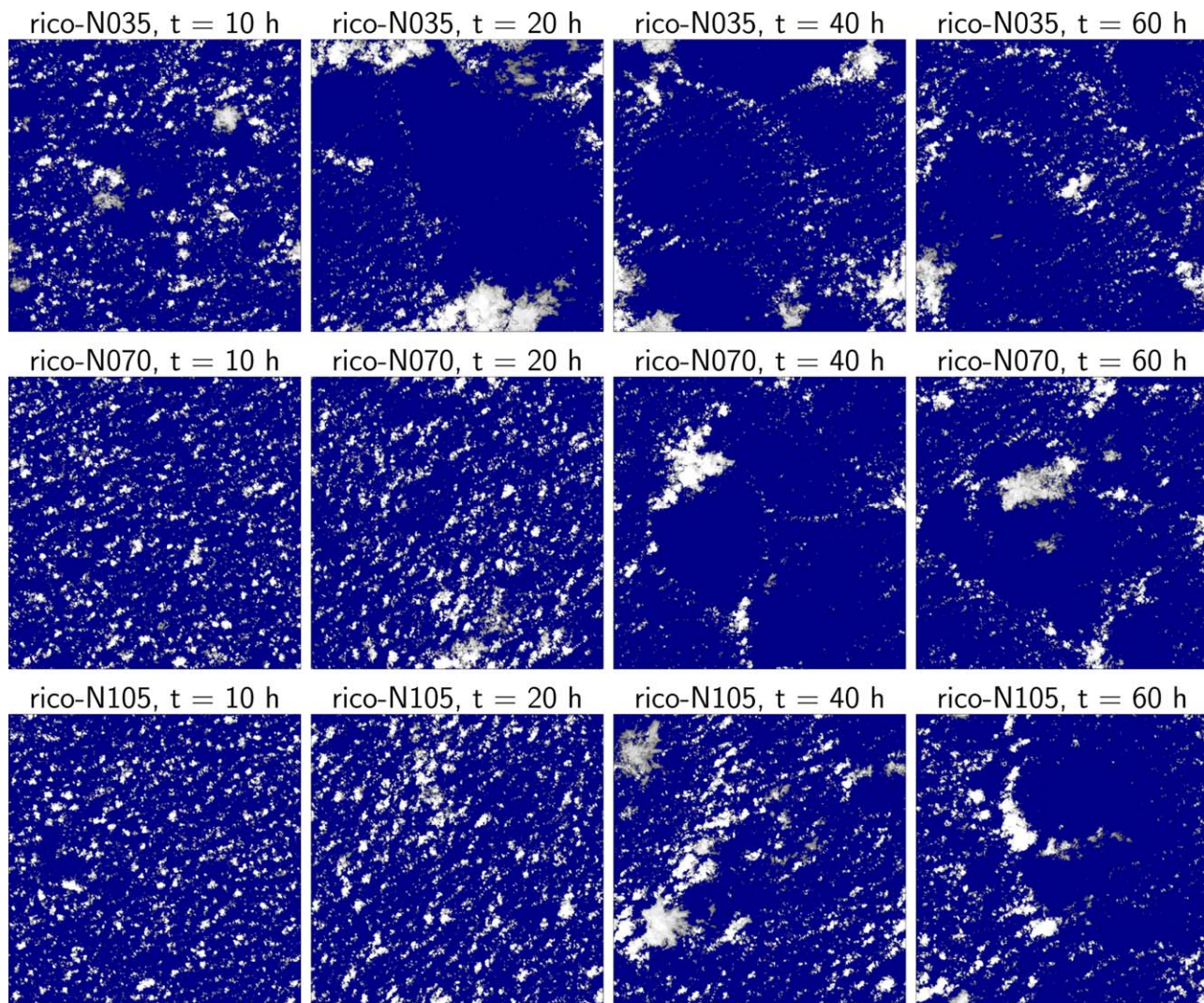
Figure 2. Plan views of albedo for three different simulations with cloud droplet number densities of 35 cm^{-3} (top row), 70 cm^{-3} (center row), and 105 cm^{-3} (bottom row) after 10, 20, 40, and 60 h (from left to right). Each plot shows an area of 50 km $\times$ 50 km. The albedo is calculated at the domain top and is representative for the whole column below.

turbulence on the resolved flow using the Smagorinsky-Lilly model. The prognostic variables are the three components of the velocity, i.e., u, v, w, the total water mixing ratio r_t, the liquid water potential temperature θ_l as well as the number and mass mixing ratios of rainwater. Cloud microphysical processes are modeled (parameterized) based on the two-moment warm rain scheme of *Seifert and Beheng* [2001] with some simplifications and refinements detailed in *Stevens and Seifert* [2008, SS08 hereafter] including the use of a constant cloud droplet number density, N, i.e., two prognostic moments are only used for rain. This approach has been shown by *van Zanten et al.* [2011] and *Ackerman et al.* [2009] to compare favorably to models employing much richer nonparametric representations of cloud microphysical processes.

The simulations setup is an idealized representation of the averaged conditions during the RICO (Rain in Cumulus over the Ocean) [*Rauber et al.*, 2007] field study as used in the GEWEX Cloud System Study (GCSS) RICO model intercomparison study [*van Zanten et al.*, 2011]. As in previous studies, we use two different initial conditions, the standard setup (labeled *rico*), which follows the GCSS configuration except for domain size and resolution, and a modified sounding with a moister cloud layer (labeled *moist*), where the latter supports a higher cloud cover and more rain early in the simulation (SS08). The GCSS setup for the RICO case includes a prescribed cooling rate designed to represent the combined effect of radiative transfer and large-scale advective cooling. The dominant contribution to the prescribed cooling is, however, from the net emission of infrared radiation from the moist trade wind layer [*van Zanten et al.*, 2011].

The grid configuration follows the benchmarks simulation of *Seifert and Heus* [2013, SH13 hereafter], but with a deeper domain. The domain size encompasses 2048 × 2048 × 200 grid points, to span a simulated volume of 51.2 km × 51.2 km × 5 km. The grid is isotropic with spacing $\Delta = 25$ m and has doubly periodic lateral boundary conditions. The deeper domain compared to SH13 proved necessary due to the depth to which some clouds grew when precipitation was suppressed, and their subsequent sensitivity to the depth of the domain if it is too shallow. In contrast to the standard RICO setup, we simulated a 60 h rather than a 24 h period. When accounting for the number of simulations (as described below) and the extended simulation time, our full suite of simulations is more than 10,000 times more computationally demanding than the simulations in the original GCSS RICO intercomparison study.

The principal aim of the study is to explore the response of the simulations to changes in N. For each configuration of model and base state, four simulations are performed with $N \in \{35, 50, 70, 105\}$ cm^{-3}. This magnitude is consistent with realistic variations of N due to both natural variability and anthropogenic changes. Measurements show that the natural variability might reach a factor of three in cloud drop number density, but is usually smaller than that [*Colon-Robles et al.*, 2006; *Gerber et al.*, 2008]. In a comprehensive study of the microphysical conditions during RICO, *Hudson and Noble* [2014] find a mean cloud droplet number density of 89 cm^{-3} with a standard deviation of 30 cm^{-3}. The impact of anthropogenic emissions on cloud droplet number densities is much smaller than the natural variability. For example, *Chen et al.* [2012] measured droplet concentrations in and outside of ship tracks in a marine environment and showed that droplet concentrations increase by 30–180%, i.e., much less than the factor of three difference spanned by our simulations. The anthropogenic perturbation to globally averaged droplet concentrations is thought to be only a few tens of percent [*Stevens*, 2015]. Hence, when interpreted as anthropogenic perturbations, the range of values we consider is large, even if not as large as explored in some other studies like *Xue and Feingold* [2006], *Xue et al.* [2008], or *Saleeby et al.* [2015].

Four additional simulations, one for each value of N, are also performed using the *rico* setup, but incorporating interactive radiation. In these simulations, the prescribed cooling is replaced by heating rates computed interactively using a variant of the broadband radiation code due to *Fu and Liou* [1992] employing Monte-Carlo spectral integration (McSI, see *Pincus and Stevens* [2009]) for computational efficiency. Local cooling rates at each time step are determined by the profile of temperature, water vapor, and cloud condensate, assuming a constant solar zenith angle of 18°. Initial simulations (denoted *irad-cool*) included an assumed advective cooling of 0.5 K d^{-1}. Because it was not clear how to best separate the effects of advective versus radiative cooling in the standard RICO setup, additional simulations were performed using interactive radiation but excluding additional advective cooling (labeled *irad-zero*).

In an earlier version of the code (including the one used by SH13), a minor bug was identified in the formulation of the sedimentation velocity. This resulted in an unintended increase in the fall speed of drizzle drops by roughly 20%. Because this has a similar effect as would a change in the shape parameter of the rain-drop distribution, we retain these simulations as a measure of the sensitivity of our results to small changes in the microphysical formulation. Three simulations, with $N \in \{35, 70, 105\}$ cm^{-3}, were performed with this older version of the code, for both the *rico* and *moist* configuration of the model. We denote these simulations by *rico** and *moist**, respectively.

Finally we explore the sensitivity of the results to a particular realization using three simulations of the *rico* case with $N = 70$ cm^{-3} which differ only in the random seed used in the random perturbation that breaks the translational symmetry of the initial state, and therefore test the sensitivity of the results to the realization of the flow.

The use of a diagnostic approach to represent the cloud-droplet spectrum allows us to focus on the effect of N on the development of precipitation. A richer palette of aerosol-cloud interactions has been hypothesized to result from differing degrees of disequilibrium between the droplet spectrum and its environment [e.g., *Feingold et al.*, 1996; *Xue et al.*, 2008; *Small et al.*, 2009]. We expect these disequilibrium effects to have a small impact on the evolution of the cloud field and have not included them in our simulations.

3. Simulations: Three Regimes of Shallow Convection

A visual impression of the cloud field as simulated by the LES is given by Figure 1, which suggests that the large spatial domain of our simulations allows for a realistic and complex structure of the simulated trade
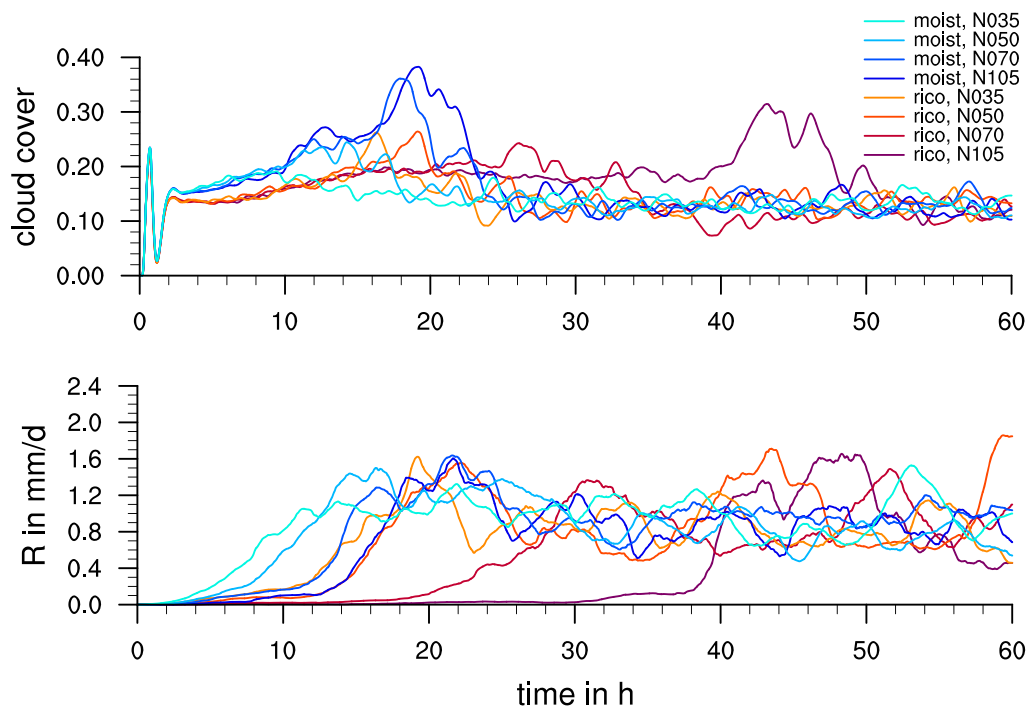
Figure 3. Time series of cloud cover and rain rate for simulations of the standard RICO case, *rico*, with different cloud droplet number densities (Simulations 1, 2, 3, and 6 in Table 1) and corresponding simulations of the moist RICO case (*moist*, simulations 7, 8, 9, 10 in Table 1).

wind cumulus cloud field. Figure 2 shows plan views of cloud albedo for three of the standard *rico* simulations with N varying by a factor of three. After 10 h, the cloud fields of all three simulations are dominated by many small clouds with relatively little evidence of spatial organization. This changes over time and all cloud fields eventually evolve into a more complex pattern with cloud free areas, regions dominated by small clouds, and larger cloud clusters with bigger clouds often aligned in arc-shaped squall lines. The late-time structure is more reminiscent of the cloud structures evident in the satellite images taken during RICO, e.g., *Rauber et al.* [2007]. This transition occurs earlier in the simulation for low N than for high N.

The transition from a random to organized cloud fields goes hand in hand with changes in the cloud cover and the surface rain rate R (Figure 3). After the first 2 h, when the effects of the spin-up of turbulence are less evident, all of the *rico* and *moist* simulations show a gradual increase in cloud cover and surface rain rate. The latter increases more rapidly with time after a few hours, particularly in those simulations for which the rain development is retarded. Depending on N, the development of substantial surface precipitation (exceeding about 0.5 mm d^{-1}) can take a few hours (for *moist* with low N) or several tens of hours (for *rico* with high N). For the simulations in which stronger precipitation develops more suddenly, there is an increase in cloud cover accompanying the development of precipitation, and a reduction of cloud cover, to values generally less than before the onset of precipitation. All simulations show pronounced rain at the end of the simulations (after 60 h) and all have a quasi-stationary cloud cover that is slightly less than before the onset of precipitation. This final regime, with significant precipitation and a slightly reduced cloud cover, corresponds to the organized cloud fields in Figure 2. The reduction in cloud cover is easily understood from the presence of large cloud free areas. The fact that all simulations reach a precipitating state with clouds organized in larger-scale structures differs from SH13, and is explained by the longer integration time and somewhat deeper model domain (5 km instead of 4 km in SH13).

Based on this behavior, it proves useful to distinguish among three stages in the temporal development of the simulations: (1) a non or very weakly-precipitating regime with no spatial organization of the cloud field; (2) a transition regime in which the rain rate increases and the cloud cover shows first an increase and then a rapid decrease; and (3) a quasi-stationary regime in which the cloud field is organized in mesoscale patterns. The regimes can be roughly separated in time by the area-averaged rain rate R. We define the

Table 1. Variables Are the Area-Averaged Albedo A, Cloud Cover C, Cloud Liquid Water Path LWP in g/m^2, Rain Water Path RWP in g/m^2, Surface Rain Rate R in mm d^{-1}, Equilibrium Rain Rate R_{eq} in mm d^{-1}, the Total Drying Rate D, Which Is the Sum of Subsidence and Advective Drying, in mm d^{-1}, and the Evaporation Rate E at the Sea Surface in mm d^{-1a}

n	Case	N_c	t_1	t_2	A	C	LWP	RWP	R	R_{eq}	D	E
1	rico	35	9.0	26.1	11.0 ± 0.8	12.8 ± 1.4	12.3 ± 2.1	12.8 ± 5.3	1.00 ± 0.6	0.82	4.60	5.42
2	rico	50	13.5	28.3	11.5 ± 1.0	13.3 ± 1.6	13.6 ± 3.1	12.6 ± 7.0	1.11 ± 0.8	0.92	4.58	5.50
3	rico	70	20.5	35.3	11.0 ± 1.1	11.6 ± 1.8	13.8 ± 3.2	10.7 ± 4.5	0.89 ± 0.5	1.22	4.57	5.78
4	rico	70	26.5	40.5	10.9 ± 0.9	11.4 ± 1.4	13.4 ± 3.5	11.6 ± 7.1	1.07 ± 0.9	1.34	4.51	5.85
5	rico	70	20.8	39.9	10.7 ± 0.7	10.9 ± 1.1	13.9 ± 2.4	12.0 ± 4.7	1.04 ± 0.6	1.29	4.53	5.82
6	rico	105	38.5	52.0	11.2 ± 0.8	12.0 ± 1.5	13.3 ± 2.7	7.3 ± 4.4	0.63 ± 0.5	1.68	4.39	6.07
7	moist	35	4.7	20.5	11.4 ± 0.8	13.5 ± 1.4	13.1 ± 2.5	14.1 ± 5.5	1.17 ± 0.6	0.89	4.14	5.03
8	moist	50	6.5	22.4	11.2 ± 0.7	12.8 ± 1.2	13.2 ± 2.4	11.8 ± 4.7	1.02 ± 0.5	0.98	4.14	5.11
9	moist	70	9.9	26.2	11.6 ± 0.9	13.0 ± 1.5	14.6 ± 2.7	11.6 ± 4.9	1.09 ± 0.6	1.07	4.13	5.20
10	moist	105	13.5	28.0	11.9 ± 1.1	12.8 ± 1.7	16.3 ± 3.6	10.7 ± 5.4	1.04 ± 0.7	1.21	4.11	5.32
11	rico*	35	9.4	25.8	11.0 ± 0.6	13.7 ± 1.1	11.9 ± 2.0	14.1 ± 5.0	1.07 ± 0.5	1.09	4.31	5.39
12	rico*	70	24.9	39.9	11.3 ± 1.0	13.1 ± 1.7	13.5 ± 2.6	12.1 ± 5.0	1.02 ± 0.6	1.28	4.51	5.79
13	rico*	105	37.0	53.5	11.8 ± 1.4	13.8 ± 2.7	15.1 ± 3.0	12.1 ± 5.8	1.05 ± 0.7	1.68	4.38	6.06
14	moist*	35	5.5	21.6	11.4 ± 0.7	14.3 ± 1.4	13.0 ± 1.8	15.3 ± 4.8	1.15 ± 0.5	0.95	4.14	5.09
15	moist*	70	7.6	25.2	12.0 ± 0.8	14.8 ± 1.4	14.6 ± 2.5	12.3 ± 5.2	1.09 ± 0.6	1.05	4.14	5.19
16	moist*	105	12.6	26.4	11.7 ± 0.9	13.4 ± 1.6	15.6 ± 3.0	10.6 ± 4.8	0.92 ± 0.5	1.17	4.12	5.29
17	irad-cool	35	4.6	23.3	10.9 ± 0.6	11.9 ± 1.2	14.0 ± 1.8	18.1 ± 5.1	1.28 ± 0.6	1.40	4.49	5.89
18	irad-cool	50	4.7	23.1	11.0 ± 0.8	11.6 ± 1.3	14.3 ± 3.0	16.6 ± 6.8	1.37 ± 0.8	1.45	4.44	5.90
19	irad-cool	70	5.4	27.0	10.6 ± 0.7	10.6 ± 1.1	14.7 ± 2.9	13.9 ± 6.1	1.11 ± 0.7	1.57	4.44	6.01
20	irad-cool	105	7.4	28.9	11.1 ± 1.0	11.0 ± 1.7	16.3 ± 3.6	11.3 ± 5.9	0.92 ± 0.7	1.64	4.40	6.04
21	irad-zero	35	5.5	24.1	9.7 ± 0.6	9.5 ± 1.2	11.4 ± 1.9	13.0 ± 4.1	0.78 ± 0.4	1.04	4.57	5.61
22	irad-zero	50	4.9	26.0	10.1 ± 0.5	10.1 ± 0.9	12.1 ± 1.9	11.6 ± 4.3	0.81 ± 0.4	1.03	4.57	5.61
23	irad-zero	70	7.2	27.6	10.0 ± 0.8	9.7 ± 1.4	12.2 ± 2.8	10.5 ± 4.8	0.84 ± 0.6	1.13	4.53	5.66
24	irad-zero	105	9.2	31.0	10.2 ± 0.8	9.6 ± 1.4	12.7 ± 3.0	8.1 ± 4.6	0.72 ± 0.6	1.13	4.50	5.63

[a]For each simulations, those variables are averaged over the quasi-stationary precipitating regime, i.e., times $t > t_2$. For some variables, the standard deviation of the time series is over this same period is provided as a measure of variability. Simulations 3–5 sample realization uncertainty using different random seeds in the initial condition.

transition between the first and second regimes as the time when R is first larger than 0.2 mm d^{-1}, and the transition to the third regime occurs 12 h after R first exceeds 0.8 mm d^{-1}.

Tables 1 and 2 summarize many properties of the simulations, with most variables averaged over the quasi-stationary regime. Many of our findings can already be anticipated from these tables, including the increase in the transition time t_2 with N (especially for the *rico* simulations) and, in the quasi-stationary regime, the

Table 2. Continuation of Table 1 Providing the Time-Averaged Values of the Latent Heat Flux LHF and Sensible Heat Flux SHF in W/m^2, Cloud Base Height z_{base} in m, Inversion Height z_{inv} in m Measured by the Maximum θ_l-Gradient, Near-Surface Wind Speed u_1 in m/s and Vapor Mixing Ratio q_1 in g/kg, the Increase of the LHF Relative to the Corresponding N035 run, Δ_{LHF} =LHF/LHF$_{N35}$ −1, in %, the Increase of the Near-Surface Moisture Gradient, $\Delta_q = (q_1 - q_{sfc})/(q_{1,N35} - q_{sfc}) - 1$, in %, the Relative Humidity in the Cloud Layer Between 900 and 1200 m, RH$_{cld}$, Integrated Water Vapor IWV in kg/m^2, and the Maximum Vertical Velocity w_{max} in m/s

| n	Case	N_c	LHF	SHF	z_{base}	z_{inv}	u_1	q_1	Δ_{LHF}	Δ_q	RH$_{cld}$	IWV	w_{max}
1	rico	35	156.8	10.3	695.8	1941.6	7.8	16.1	0.00	0.00	88.2	35.61	10.7
2	rico	50	159.2	9.7	719.6	2024.1	7.8	16.0	1.52	1.56	87.4	35.72	10.7
3	rico	70	167.3	8.8	773.1	2313.8	7.8	15.7	6.72	7.00	85.1	36.24	12.5
4	rico	70	169.3	8.9	792.5	2309.7	7.8	15.6	8.00	8.27	84.2	36.26	12.1
5	rico	70	168.4	8.9	778.6	2359.4	7.8	15.7	7.43	7.91	84.1	36.31	12.5
6	rico	105	175.5	7.9	881.8	2616.0	7.8	15.4	11.97	11.94	82.2	36.72	13.3
7	moist	35	145.7	10.3	635.8	1850.0	7.8	16.5	0.00	0.00	89.3	40.66	9.8
8	moist	50	148.0	9.3	655.4	1928.5	7.8	16.5	1.59	1.50	88.4	40.78	10.5
9	moist	70	150.5	8.7	685.7	2073.7	7.8	16.4	3.33	3.13	87.6	40.96	11.0
10	moist	105	153.9	7.8	737.3	2277.2	7.8	16.2	5.68	5.36	85.9	41.20	12.1
11	rico	35	156.0	10.5	660.0	1896.2	7.8	16.2	0.00	0.00	88.2	34.50	10.1
12	rico	70	167.5	9.1	797.9	2199.5	7.7	15.7	7.32	9.04	85.2	36.11	11.0
13	rico	105	175.2	8.3	891.0	2555.9	7.7	15.4	12.28	14.15	81.7	36.60	12.9
14	moist	35	147.2	10.4	626.2	1836.1	7.8	16.5	0.00	0.00	89.7	38.51	9.7
15	moist	70	150.2	8.8	695.2	1972.8	7.8	16.4	2.06	2.10	87.8	40.88	10.5
16	moist	105	153.1	7.8	711.5	2246.8	7.8	16.3	3.99	4.28	86.4	41.15	11.9
17	irad-cool	35	170.6	11.1	769.4	2299.4	7.8	15.6	0.00	0.00	86.7	35.86	12.1
18	irad-cool	50	170.7	10.3	776.1	2289.6	7.8	15.6	0.05	0.00	85.5	35.87	12.1
19	irad-cool	70	174.0	9.2	793.8	2508.3	7.8	15.5	2.01	2.11	83.7	36.18	13.7
20	irad-cool	105	174.7	8.3	828.8	2667.6	7.8	15.5	2.40	2.53	82.2	36.44	14.8
21	irad-zero	35	162.3	8.0	730.5	2331.0	7.8	15.9	0.00	0.00	85.4	35.89	12.6
22	irad-zero	50	162.2	7.3	756.7	2354.6	7.8	15.9	−0.07	0.05	84.6	35.91	12.7
23	irad-zero	70	163.8	6.6	771.0	2446.4	7.8	15.9	0.90	1.06	82.8	36.12	13.5
24	irad-zero	105	163.0	5.7	768.6	2526.0	7.8	15.9	0.43	1.00	81.5	36.21	14.1
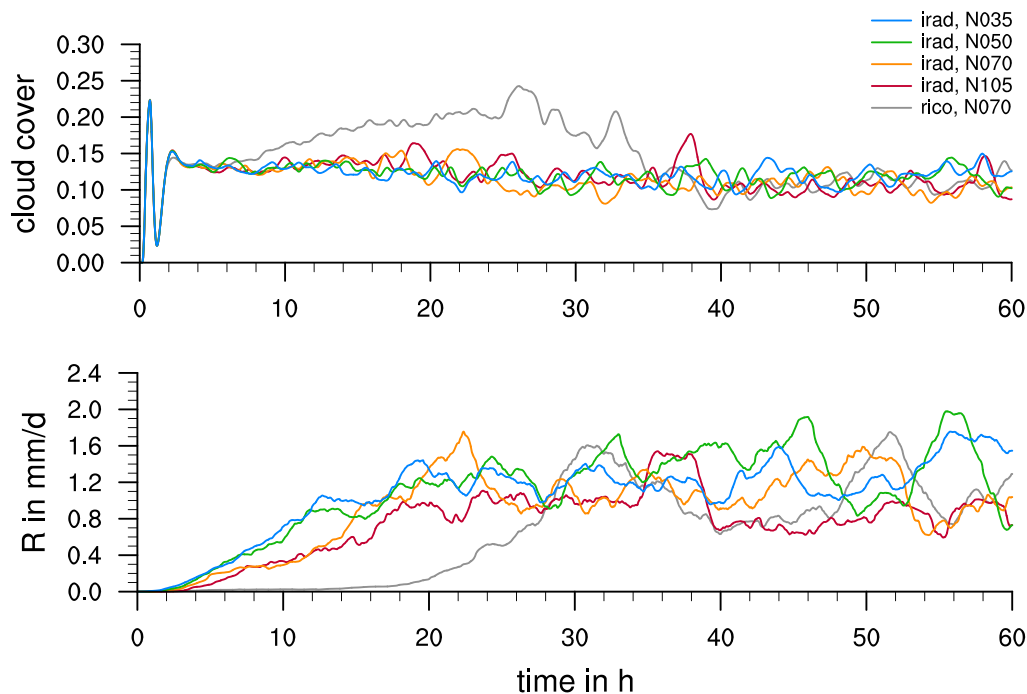
Figure 4. Time series of cloud cover and rain rate for simulations of the RICO case with interactive radiation, *irad-cool*, for different cloud droplet number densities (Simulations 17, 18, 19, and 20 in Table 1) and the *rico*-N070 simulation (no. 3) for comparison.

tendency for larger LWP and smaller RWP with larger N, with relatively weak dependence of cloud cover. Similar behavior has been seen in previous LES studies, e.g., by *Xue and Feingold* [2006], *Lee et al*. [2012], and *Bretherton et al*. [2013], but those earlier results might have been more difficult to interpret due smaller domain sizes and shorter integration times. The results of our simulations will be discussed in detail in the following sections.

The set of simulations includes experiments with different random seeds leading to different fluctuations in the initial condition. This has little effect on the quasi-stationary regime but can significantly affect the initiation of significant precipitation, and hence the timing of regime transitions, as both t_1 and t_2 can vary by several hours depending on the realization.

The simulations with interactive radiation have a very different time evolution (Figure 4). The increase in cloud cover during the transition regime is missing in the *irad* simulations compared to the corresponding *rico* simulations. In addition, the simulations with higher N develop precipitation much earlier than their *rico* counterparts, i.e., the transition time t_2 is reduced and depends much less on N than in the *rico* simulations (recall that all *irad* simulations have the same initial condition as *rico*, not the higher moisture as in *moist*). With interactive radiation, the model obviously develops rain much more readily, a point we return to in section 6.

Thus the simulations suggest that important macroscopic properties of the boundary layer and its cloud field come into rough statistical equilibrium with the forcing relatively quickly—within roughly a day for the *irad-cool* family of simulations. The timescale for this approach to stationarity depends in general on the development of precipitation, although this dependence is weaker when radiative cooling interacts with the local environment.

Temporal fluctuations of cloud properties in the quasi-stationary regime, as measured by the standard deviation of the time series, are larger than any systematic difference across a family of simulations (which differ only in the prescription of N). Considering the three different realizations of *rico* with $N = 70$ cm^{-3} and different random seeds suggests that using the standard deviation to measure the uncertainty of the mean likely exaggerates the uncertainty; but even assuming that uncertainty in the mean is a factor of two or three smaller than the standard deviation in the mean, differences in important quantities as a function of N are difficult to establish. In other words, the distribution of cloud properties in the quasi-stationary regime in our
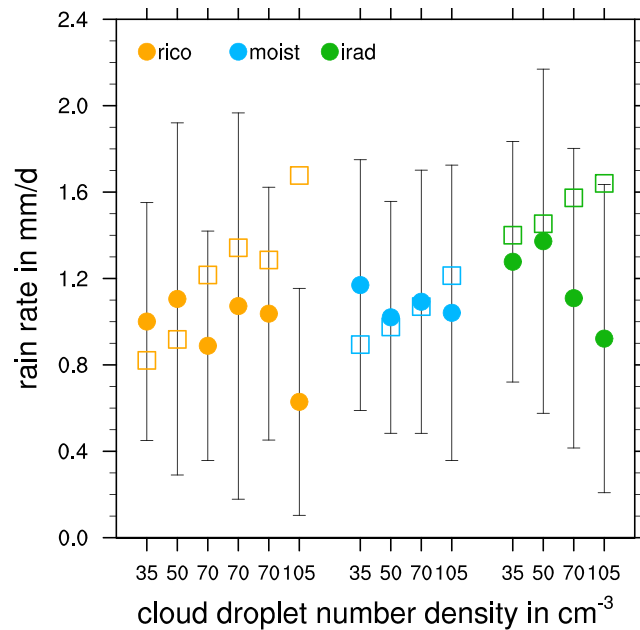
Figure 5. Averaged rain rate (bullets, with standard deviation as error bars) and equilibrium rain rate (open boxes) for simulations 1–6 (*rico*, orange), 7–11 (*moist*, blue), and simulations 17–20 with interactive radiation (*irad-cool*, green).

simulations shows no statistical significant dependency of N. Although a small effect cannot be ruled out, the lack of a strong effect is consistent with physical arguments developed in the remainder of this paper.

4. Subsiding Radiative-Convective Equilibrium

It is useful to think of the quasi-stationary regime as a generalization of radiative-convective equilibrium (RCE). In the classical formulation of RCE, convective heating balances radiative cooling of the atmosphere while precipitation balances evaporation at the surface [*Ramanathan and Coakley*, 1978]. Here prescribed subsidence and advective forcings, representing the effects of the large-scale circulation, add additional moisture and heat sources that reduce the rain rate that is required relative to pure RCE (see, e.g., *Popke et al.* [2013] for further references and a short historical perspective on RCE). To emphasize the role of subsidence and distinguish the present configuration from the more idealized case of pure RCE, we refer to the stationary state as Subsiding RCE, or SRCE. In SRCE shallow, rather than deep, convection predominates.

In SRCE, surface rain rate must balance the sum of surface evaporation E, drying due to subsidence, D_W, and large-scale moistening (or drying) from horizontal advection M_{adv},

$$R_{eq} = E - D_W + M_{adv}$$
$$= E - \int_0^\infty W \frac{\partial q_t}{\partial z} dz + M_{adv}. \tag{1}$$

For an atmosphere in which the divergence is constant, the equilibrium rain-rate can be cast at a function of a large-scale moistening which is prescribed (both through the specification of advective moistening assuming a prescribed surface property and mean 10 m wind) such that (see Appendix A)

$$R_{eq} = M - \mathcal{D}Q(1+\gamma), \tag{2}$$

where here Q is the integrated total water within the turbulent layer, $\mathcal{D}$ the large-scale divergence, and M a prescribed moistening rate which is dominated by the state-independent part of the surface evaporation. The γ term is a dimensionless parameter that depends on the ratio of the subsidence velocity at the top of the layer to the surface exchange velocity as well as the ratio between the near surface humidity and the mean humidity in the layer. In strict RCE, M would only contain the evaporative component, and $\mathcal{D}$ would be zero. For the RICO case, wherein the subsidence profile is artificially decoupled from the state of the layer so that it remains constant above a certain height the stationarity relationship, equation (2), becomes a little more complicated, but does not fundamentally change its character.

Equation (2) shows that in stationarity the rain rate depends on the moistening rate and the amount of integrated total water in the domain. Because the rate of drying from large-scale subsidence increases with the amount of moisture in the layer, moister layers experience a stronger subsidence drying and thus need to rain less to balance the water budget. Figure 5 compares the equilibrium rain rate (calculated from equation (1)) with the time-averaged rain rate during the quasi-stationary regime for the *rico*, *moist*, and *irad-cool* simulations, i.e., for $t > t_2$. For most of the simulations, the actual rain rate is close to the value expected for

stationarity. Only for the simulations with large values of N, which have the most delayed approach to stationarity do deviations from stationarity become apparent.

Another striking result of Figure 5 is that the equilibrium rain rate increases with increasing drop number, and this is shown robustly by the different sets of simulations. Based on the budget analysis as expressed by equation (2), one can speculate whether or not in stationarity the mean state adjusts to the present precipitation rate, i.e., the layer moistens so that Q increases to balance M, or if R_{eq} increases. Physically it is hard to imagine how the increase in Q, which is necessary for the high N simulations to come into stationarity, would not lead to R_{eq} also increasing. The somewhat drier transient state implied by $R < R_{eq}$, particularly for those simulations which take the longest to come into stationarity is also consistent with the development of a deeper cloud layer through the adjustment process. More rapid deepening of the cloud layer in the approach to stationarity is expected to mix more warm and dry air to the surface, thereby increasing latent heat fluxes, i.e., surface evaporation, and reducing sensible heat fluxes.

The increase in the surface evaporation that accompanies an increase in N also follows from bulk formula which parameterizes surface fluxes. Following the GCSS RICO setup, we use the surface flux relationship given by

$$\overline{w'q'_t} = -C_q u_1 (q_1 - q_{sfc})$$ (3)

with $C_q = 0.001133$ and u_1 and q_1 being the wind speed and total water mixing ratio in the lowest model level. As q_{sfc} is a fixed surface value at an SST of 299.8 K, an increase in E can only be caused by either an increase in u_1 or a decrease in q_1 (note that $q_1 < q_{sfc}$ for an upward flux). As shown in Table 2, the average wind speed does not change with N, but q_1 does. The decrease in the near-surface moisture (and relative humidity) fully explains the increase in E as shown by the matching relative increase in both variables (see Table 2).

5. Dynamical Responses to Precipitation and the Buffering of Aerosol Effects

The bulk arguments in section 4 suggest that the equilibrium rain rate should increase and relative humidity decrease, with increasing N. In this section, we further explore the mechanisms by which this balance is struck.

5.1. Inhibiting Precipitation Leads to Deeper Clouds
An increased cloud droplet number density makes collisional processes among droplets less efficient and thus delays the onset of rain. Clouds in which the rain onset is sufficiently delayed will evaporate before rain develops, and thus will not precipitate. For the *Seifert and Beheng* [2001] autoconversion rate used in our simulations, a doubling of N leads to a reduction of the conversion rate from cloud droplet to rain by a factor of 4. Hence as N increases autoconversion increasingly becomes a bottleneck for rain formation. As we have seen, the trade wind cumulus system finds ways to counteract and overcome this microphysical inhibition and eventually all simulations reach a similar rain rate independent from the assumed cloud droplet number density. This is expected from the bulk constraints of SRCE.

The dominant response of cloud layers to larger N and a suppression of rain formation is to grow deeper [*Stevens and Seifert*, 2008; *Blossey et al.*, 2013; *Bretherton et al.*, 2013]. In our simulations, inversion height z_i, measured by the location of the maximum θ_r-gradient, increases from below 2000 m at a droplet number density of 35 cm^{-3} to more than 2600 m for 105 cm^{-3}. Cloud base also rises from about 700 to 900 m but this is a much smaller effect. This increase in the depth of the layer through which clouds mix is associated with an increase in cloud cover throughout the approach to stationarity. However, once precipitation develops sufficiently for the layer to reach the quasi-stationary regime, cloud cover and the overall albedo does not depend on the depth of the layer or on N.

Instead it is systematic changes in the internal structure of the cloud layer that mark the influence of the dynamical response, i.e., the deepening of the cloud layer, to perturbations in N. Figure 6 shows the profiles of cloud fraction, cloud water mixing ratio, relative humidity, and the flux of total water in the quasi-stationary regime. Cloud fraction shows the typical trade wind cumulus profile with a maximum at cloud base [cf. *Nuijens et al.*, 2014], a decrease with height, and a second local maximum at the top of the cloud layer. Both the rise of cloud base height and the increase in the depth of the cloud layer with increasing N
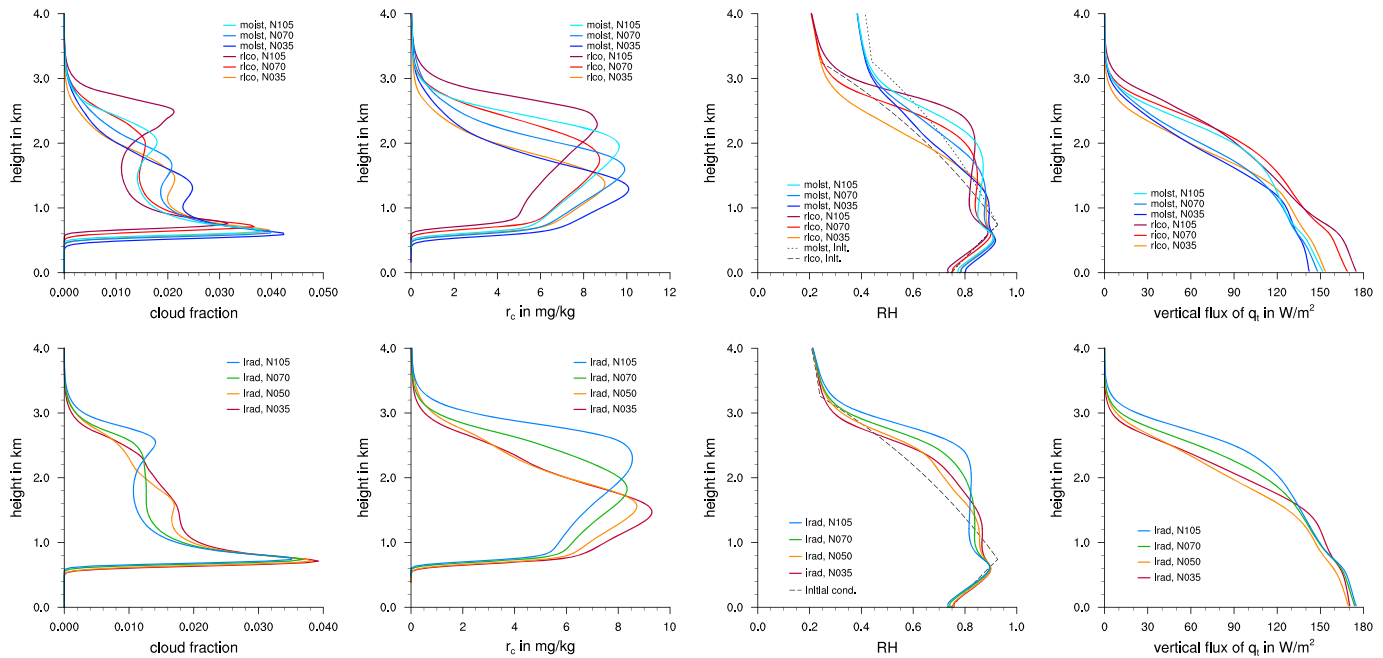
Figure 6. Domain-averaged profiles of cloud fraction, cloud water mixing ratio, relative humidity, and the flux of total water. Shown are the standard RICO case (*rico*, light to dark blue, upper row) and the moist RICO case (*moist*, orange-red, upper row) and the *irad-cool* simulation with interactive radiation (lower row). Profiles are averaged in time over near-equilibrium regime, i.e., after time t_2.

are evident. The deepening of the cloud layer with increasing N is most apparent in the profiles of cloud liquid water mixing ratio which shows a clear maximum in the upper part of the layer.

The change in thermodynamic structure with increasing N is mediated by a small part of the total cloud population, namely the deepest and most actively precipitating clouds. The deepening of the cloud layer is mostly caused by the transport and mixing due to the largest and deepest congestus-type clouds that penetrate into the inversion layer, and correspondingly those are the clouds that also change strongest with increasing N. Histograms of cloud top height in the quasi-stationary regime shown in Figure 7 clearly identify two cloud modes: a large number of shallow clouds with cloud top heights below 1000 m height, and a second mode of deeper clouds. As N increases the shallow mode remains largely unchanged but the deeper mode gets even deeper. Additional analysis (not shown) confirms that it is this deep cloud mode that produces almost all precipitation. These deeper clouds are also the most vigorous: Figure 8 shows that
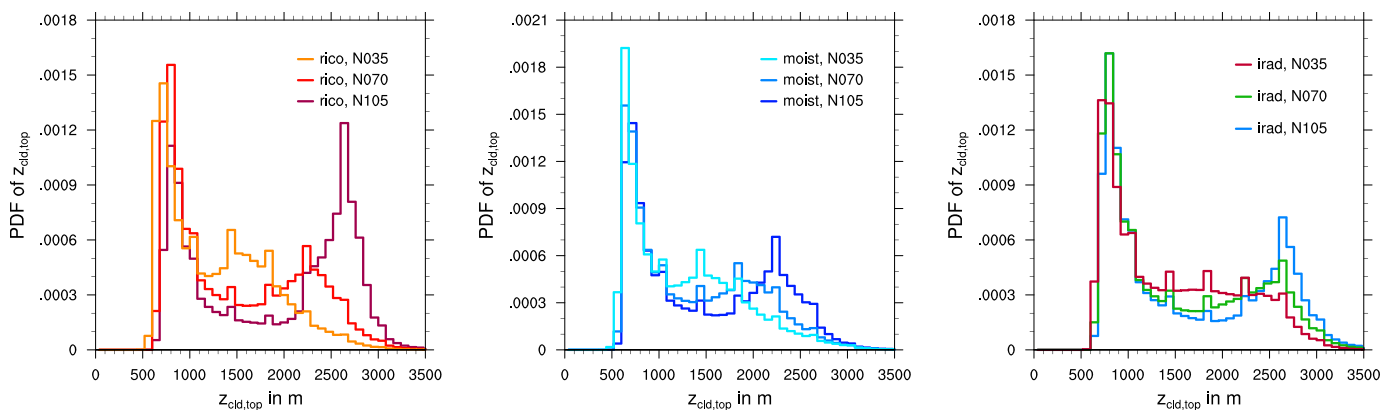

Figure 7. Probability density functions of the cloud top height for the standard RICO simulation (left), the moist RICO case (center), and the *irad-cool* simulations with interactive radiation (right).
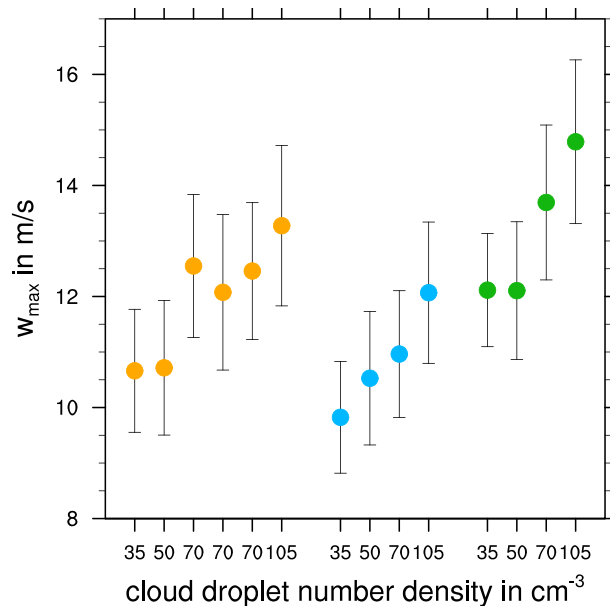
Figure 8. Time-averaged domain-maximum vertical velocity during the near-equilibrium precipitating regime. Shown are simulations 1–6 (standard RICO, orange), 7–11 (moist RICO, blue), and *irad-cool* simulations 17–20 with interactive radiation (green). Error bars provide the standard deviation of the time series.

domain-maximum vertical velocity increases with N and hence the depth of the deepest clouds. This behavior is consistent with the observations of, e.g., *LeMone and Zipser* [1980], who show that the upper decile of vertical velocities in deep clouds increase linearly with height above cloud base through the lower 4 km of the cloud.

This implies that changes in N primarily affect the growth of the deepest and most vigorous clouds. The invigoration of these clouds leads to deeper boundary layers, as by delaying the onset of precipitation these clouds can continue to loft their condensate into the inversion and thus grow deeper with time [*Stevens*, 2007]. Stronger updrafts are more effective in lofting condensate and deepening the cloud layer if they do not precipitate and, should precipitation develop, they can loft precipitate and thereby more effectively convert cloud water to rain.

Growing deeper clouds thus offsets the microphysical bottleneck that would otherwise narrow as N increases. Deeper clouds produce higher cloud water contents and, because the SB2001 autoconversion rate depends sensitively on cloud water mixing ratio, an increase in cloud water content can counteract the effects of an increasing N on autoconversion. For the prescribed conditions of SRCE, the development of precipitation is demanded by the large-scale forcings, and deepening of the cloud layer is an efficient way to meet this demand and bring the boundary layer into a state of quasi-stationarity.

5.2. Inhibiting Precipitation Leads to Drier Boundary Layers

The drying that accompanies the deepening of the cloud layer, and which is expected based on the quasi-stationary response discussed earlier, is evident throughout the layer (see the profiles of relative humidity in Figure 6). The drier subcloud layer is consistent with a more elevated lifting condensation level of the subcloud layer air, and a higher cloud base, and also explains the increase in the latent heat flux. By suppressing the development of precipitation, more condensate is lifted into the stable trade wind inversion. The evaporative cooling of the condensate in this layer progressively destabilizes it, allowing for its eventual incorporation into the cloud layer; in simulations with interactive radiation, the moister air near the inversion also cools more quickly. This deepening mechanism is effective so long as the profile of moist static energy decreases with height, which is the case in the lower troposphere within the trades. If the moist static energy decreases sufficiently, the air above the inversion will be dry enough that upon being incorporated into the trade wind layer, even after moistening through condensate evaporation, it is drier than the cloud layer itself. As a result, net drying accompanies the deepening, even though through the transient adjustment the loss of condensate to precipitation is reduced. This drying is evident throughout the cloud layer as N increases and the layer deepens. Deeper layers are drier. This decrease in RH contributes to a reduction of the cloud fraction near cloud base, i.e., reduced number of small clouds for higher N, Figure 7. And overall we find a small decrease in cloud cover for higher N (Table 1). These results are consistent with the CGILS S6 simulations of *Bretherton et al.* [2013], their CTL versus N25.

Some of the seemingly paradoxical behavior can be resolved by pointing out that the high N simulations are only drier in terms of RH and especially in certain height levels, like near cloud base or near the surface.
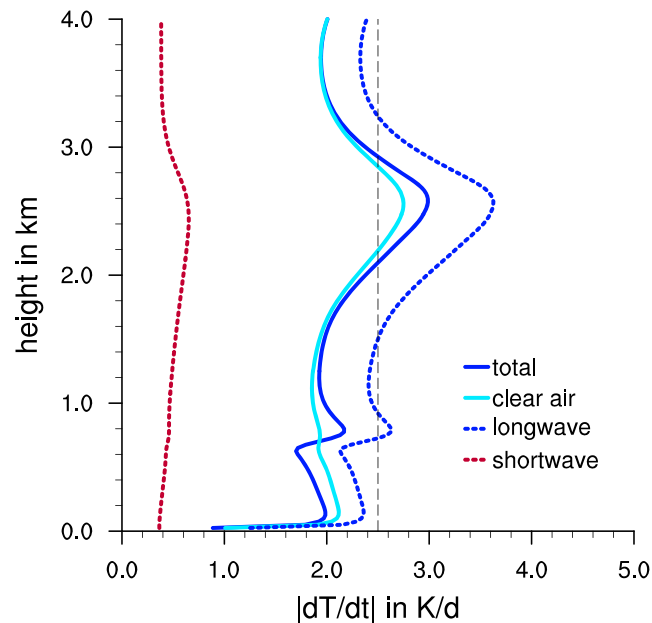
Figure 9. Vertical profiles of the total radiative cooling rate (solid dark blue), the long-wave radiative cooling rate (blue-dashed), and the short-wave heating rate (red-dashed), and the clear-sky long-wave cooling rate (solid light blue). Shown is a time average of the *irad-cool*-N070 simulation for the quasi-stationary regime ($t > t_2$). Note that the profiles are only shown up to a height of 4 km, and above that we blend the total cooling rate to the value of 2.5 K/d, which is required to be consistent with the upper boundary condition and subsidence rate of the RICO case. The black-dashed line represents the constant cooling rate of 2.5 K/d of the GCSS RICO setup.

In terms of integrated moisture quantities like IWV or Q, the high N simulations are actually marginally moister than their low N counterparts, i.e., while RH_{cld} is decreasing IWV is increasing for higher N (Table 2).

The deepening of the cloud layer to overcome microphysical inhibition is an example of what *Stevens and Feingold* [2009] call buffering (e.g., their Figure 4), in which systems in which aerosols are perturbed exhibit dynamical changes that mute initial aerosol effects. We will see later that the decrease in RH within the cloud layer, which accompanies its deepening, adds another twist to this buffering mechanism.

6. Radiative Feedback and the Approach to Equilibrium

In the *rico* and *moist* simulations, radiative cooling is specified and held constant with height consistent with the GCSS case specifications and other simulations of trade wind cumulus. This is a poor assumption, especially when the free atmosphere is very dry, because radiative cooling is dominated by the vertical distribution of water vapor, with maximum values where the (broadband) clear sky optical depth measured from the top of the atmosphere is near unity. Indeed, clear-sky radiative cooling for the soundings used in the present simulations shows a distinct vertical profile, with the clear-sky cooling maximizing near the height of the maximum vertical gradient of water vapor. As Figure 9 shows, the radiative cooling as calculated by the interactive radiation scheme is largest at about 2.5 km height, near the trade wind inversion. This cooling peak has an additional contribution from clouds, evident in the difference between the clear-air and total irradiance, but sensitivity studies (not shown) confirm that clear sky radiation plays the dominant role in the dynamics and evolution of the layer. Strong radiative cooling localized in the upper cloud layer destabilizes the layer and invigorates convection (i.e., the maximum updraft velocities are larger in simulations with interactive radiation, Figure 8). More penetrative updrafts, combined with more cooling directly in the inversion as condensate evaporates and moistens this layer, accelerate the deepening of the cloud layer. This is why simulations with interactive radiation approach quasi-stationarity much more rapidly (see Figure 4), and with greatly reduced dependence of t_2 on N (Table 1), than do simulations in which radiative cooling is prescribed.

Given only the *rico* and *moist* simulations, it could be argued that that the primary effect of changes in the aerosol is to delay the onset of precipitation, resulting in a longer-lived phase of nonprecipitating convection in which cloud cover increases slightly with N. This would appear to have a large potential impact: a threefold increase in N can delay the onset of precipitation by more than a day in a dry free atmosphere (Table 1). Given a mean wind of 10 m s^{-1}, this corresponds to a fetch of nearly a thousand kilometers, and thus could affect the optical properties of the cloud field over a modestly large area.

But this sensitivity is unlikely to be present in nature. When radiative cooling is applied consistent with the time-evolving distribution of water vapor and temperature, differences in the transition time to the quasi-stationary state are reduced by a factor of three or four, greatly diminishing even the transient effects of a changing aerosol environment. Simulations were not performed with interactive radiation for *moist* profiles, for which the contrast between interactive and prescribed radiation might be muted by the smaller

moisture contrast at the inversion, but the *moist* simulations also transition to their quasi-stationary state more readily, so there is less effect of N on the transient evolution to begin with.

Realistic radiative cooling, as provided by the interactive radiation using McSI, makes the buffering by the deepening and drying of the layer in response to a suppression of precipitation more effective. This further diminishes the influence of the initial microphysical perturbation on the structure of the cloud field and the final precipitation rate. We speculate that in nature, where the subsidence itself is linked to the cooling, this even more tightly coupled subsiding radiative-convective system might be even more resilient to microphysical perturbations.

7. Quantifying the Radiative Effects of Aerosol-Cloud Interactions

Our simulations allow us to quantify the change in albedo for a given change in N but, to better understand the response of the system, it is helpful to decompose the change in albedo into contributions from different processes. For instance, all else being equal an increase in N increases the albedo, as first pointed out by Twomey. Macroscopic changes of the clouds, perhaps associated with an influence of N on the lifetime of clouds, may also influence the albedo. In this section, we explore the extent cloud-macrophysical versus cloud-microphysical changes influence the albedo. We do so by exploring the sensitivity of the albedo to N, as well as indirectly through changes to the liquid water path, L_c, and cloud cover, C. (We investigate the extent to which the macrophysical changes are controlled by lifetime in section 8.)

As a starting point, we assume that albedo can be expressed in terms of a bulk cloud amount and liquid water path, such that

$$A = C \frac{\tau}{\beta + \tau} + (1 - C) A_b, \tag{4}$$

where $\beta = 6.8$ [*Zhang et al.*, 2005] depends on the degree of forward scattering by cloud droplets, and the background albedo A_b is assumed to be that of the sea-surface at high-sun angles and set to 5%. The optical thickness τ is calculated following *Zhang et al.* [2005] as

$$\tau = \alpha N_c^{1/3} L_c^{5/6}, \qquad \alpha = 0.19. \tag{5}$$

We aim for a decomposition of the aerosol indirect effect into its separate contributions from changes in N directly (which we call the Twomey effect), liquid water path, L_c, and cloud cover, C. Taking the total derivative of A leads to

$$\Delta A = \left. \frac{\partial A}{\partial N_c} \right|_{L_c, C} \Delta N_c + \left. \frac{\partial A}{\partial L_c} \right|_{N_c, C} \Delta L_c + \left. \frac{\partial A}{\partial C} \right|_{N_c, L_c} \Delta C.$$

Although the evaluation of the individual terms in this expression is straightforward for small perturbations for homogeneous cloud elements, the nonlinearity in the expression of the albedo combined with large-amplitude of the changes in N in the simulations pose some challenges [cf. *Cahalan et al.*, 1994]. Here we therefore apply the approach as detailed in the following.

As a starting point, we consider how changes in the probability distribution function of the liquid water influences the domain-averaged albedo. We use a log binning of L_c, defining $\mathcal{P}(\log L_c)$ as

$$L_c = \int_0^\infty L_c' \, \mathcal{P}(\log L_c') \, \mathrm{d}\log L_c' \tag{6}$$

Next, for large N perturbations as in our simulations, we rewrite the domain-averaged albedo with help of equation (6) as

$$A = C \int_0^\infty \frac{\tau}{(\beta + \tau)} \mathcal{P}(\log L_c) \, \mathrm{d}\log L_c + (1 - C) A_b \tag{7}$$

and arrive at the following equations to evaluate the aerosol effects associated with changing N directly, and from changes in L_c and C that arise from a change in N as:
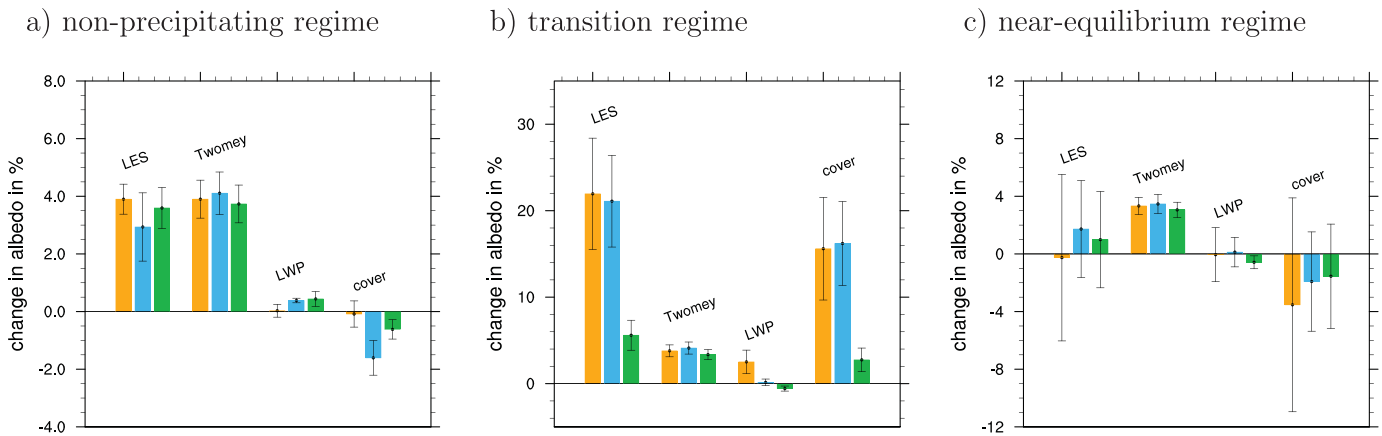
Figure 10. Estimates of the total and individual aerosol-cloud effects for a doubling of the cloud droplet number density for the non-precipitating regime (left), transition regime (center), and near-equilibrium precipitating regime (right). Colors identify three different sets of simulations: standard RICO (orange), moist RICO (light blue), and simulations with interactive radiation (green). The total effect as simulated by the LES is denoted by "LES," the individual effects are the Twomey effect, i.e., the albedo change solely attributed to cloud droplet number density. The LWP and cloud cover effect are the indirect effects, i.e., changes of liquid water path or cloud cover due to a doubling of cloud droplet number density (see text for details).

$$\Delta A_{\mathrm{T}} = \bar{C} \int_0^\infty \left(\frac{\tau_2}{(\beta+\tau_2)} - \frac{\tau_1}{(\beta+\tau_1)} \right) \overline{\mathcal{P}}(\log L_c) \mathrm{d}\log L_c$$

$$\Delta A_{\mathrm{L}} = \bar{C} \int_0^\infty \frac{\bar{\tau}}{(\beta+\bar{\tau})} \left(\mathcal{P}_2(\log L_c) - \mathcal{P}_1(\log L_c) \right) \mathrm{d}\log L_c$$

$$\Delta A_{\mathrm{C}} = \Delta C \int_0^\infty \frac{\bar{\tau}}{(\beta+\bar{\tau})} \overline{\mathcal{P}}(\log L_c) \mathrm{d}\log L_c - \Delta C A_b$$

with

$$\tau_i = \alpha N_{c,i}^{1/3} L_c^{5/6}, \qquad \bar{\tau} = \alpha \bar{N}_c^{1/3} L_c^{5/6},$$

$$\bar{N} = \frac{1}{2}(N_1 + N_2), \quad \bar{C} = \frac{1}{2}(C_1 + C_2),$$

and

$$\overline{\mathcal{P}}(\log L_c) = \frac{1}{2} \left(\mathcal{P}_1(\log L_c) + \mathcal{P}_2(\log L_c) \right).$$

This approach allows us to evaluate the differences between two simulations directly, instead of making use of derivatives, but similarly to the infinitesimal analysis we hold two of the three parameters constant in each term. Essentially we ask to what extent differences in albedo can be explained by differences in N, L_c and C, respectively. For example, we hold C and $\mathcal{P}(\log L_c)$ constant in the Twomey effect by using the average values $\bar{C}$ and $\overline{\mathcal{P}}(\log L_c)$ of the two simulations.

The results of this decomposition are shown in Figure 10 for the three stages of evolution defined by t_1 and t_2. For each set of simulations (*rico*, *moist* and *irad*), we have used all available simulations as listed in Tables 1 and 2, but differences are only evaluated between comparable simulations (i.e., simulations with the same forcing, the same model version, etc.). For all pairs of simulations, the difference is then rescaled to a doubling of the cloud droplet number density. The whiskers in Figure 10 delineate the standard deviation of the independent AIE estimates. Uncertainty in cloud variables (as might be measured by the standard deviation of the mean) is not propagated through to the AIE estimates. Therefore the whiskers provide a lower bound on the uncertainty in estimates of the degree to which different terms contribute to changes in the albedo of the cloud field.

During the non- or weakly-precipitating regime ($t < t_1$), aerosol-cloud interactions are dominated by the Twomey effect, i.e., the brightening of the cloud due to more numerous but smaller droplets. Changes in the LWP are small (and positive) and changes in cloud cover are also small (but negative).

In the quasi-stationary regime ($t > t_2$), the net radiative effect from aerosol-cloud interactions is small. In this regime, the positive Twomey effect is compensated by a negative change in cloud cover while the LWP effect is still negligible. The reduction in cloud cover is small, and more uncertain than the Twomey effect, but robustly occurs for all three configurations.

In both the *rico* and *moist* set of simulations, the transition regime ($t_1 < t < t_2$) shows a marked sensitivity to changing droplet concentrations. In this regime, the Twomey effect is similar to that for the nonprecipitating regime, but cloud-cover increases substantially as the clouds deepen (but have not yet begun to precipitate) with increasing N. This change in cloud cover leads to large (approx. 20%, Figure10b) changes in the albedo. It is notable however that the simulations with interactive radiation, which have a much shorter transition regime, also show only a very small but also positive cloud cover effect during the period of transition. Unlike the simulations without interactive radiation, their response remains dominated by the Twomey response also during the transition period.

The negative cloud cover effect in the near-equilibrium precipitating regime is due to the decrease in cloud cover for higher N. This response is also evident in Table 1, although internal variability and inconsistent averaging times might raise the question as to whether the decrease in cloud cover is a statistical artifact. We do not think so, because the decrease in cloud cover is consistent with the understanding of the response of the system to an increase in N. As has been discussed in sections 4–6, clouds deepen in response to a suppression of precipitation and this results in a decrease in relative humidity, especially above cloud base (RH_{cld} in Table 2). This decrease in relative humidity reduces the number of small clouds and it reduces the size and lifetime of the cloud remnants, i.e., the cloud that is left behind after the convective cloud has rained out.

We speculate that there may also be a microphysical argument for smaller cloud remnants (or detritus) at high N. With low N rain can already form at mid-levels, but for high N the autoconversion rate is large only in the uppermost part of the cloud and rain forms there. Clouds that develop rain only at the very top are more effective in depleting the cloud water by accretion, as the raindrops fall through the whole cloud. Therefore it seems plausible that clouds that readily form precipitation, for instance because N is small, leave behind larger and thicker remnants than clouds at high N. Nevertheless, this may be a second-order effect compared to the lower relative humidity for high N, which leads to faster evaporation of the remnant (even if it has a similar size and liquid water content).

A negative cloud cover effect would imply a negative lifetime effect, i.e., clouds should have shorter lifetimes for higher N, not larger lifetimes as often assumed following *Albrecht* [1989]. We take up this question in the next section.

8. Cloud Tracking to Identify Lifetime Effects

To explore how the lifetime of simulated clouds are influenced by changes in N, we apply the cloud tracking algorithm developed by *Heus and Seifert* [2013]. For an organized cloud field like precipitating shallow convection, the definition and identification of individual clouds are not a trivial problem and has no unique solution. Using only a liquid water path threshold identifies the largest and very long lived cloud clusters as single objects, a solution that is neither physical nor useful. An advantage of the algorithm developed by *Heus and Seifert* [2013] is that cloud clusters are further decomposed into subclouds, which can be attributed to active cloud cores or updrafts. A similar decomposition has been suggested and applied earlier by *Dawe and Austin* [2012]. Four cloud types are identified: passive clouds, which have no active cloud core; isolated clouds with only one active core; clouds with an active core that are part of a cluster; and passive remnants, which are outflow regions of a multicore cloud cluster. Here we apply the cloud tracking to the last 20 h of the *irad-cool* simulations with different N.

Figure 11 shows the probability density distribution of cloud sizes, depths, and lifetimes. The cloud size distribution follows a power law for small clouds, exhibits a scale break at about 1 km size, and seems to continue as a power law for larger sizes. A similar scale break has been identified in simulations [e.g., *Neggers et al.*, 2003] and also in observations through the analysis of echo objects as measured during RICO [*Trivej and Stevens*, 2010], although quantitative the details of the scale break depends somewhat on the details of
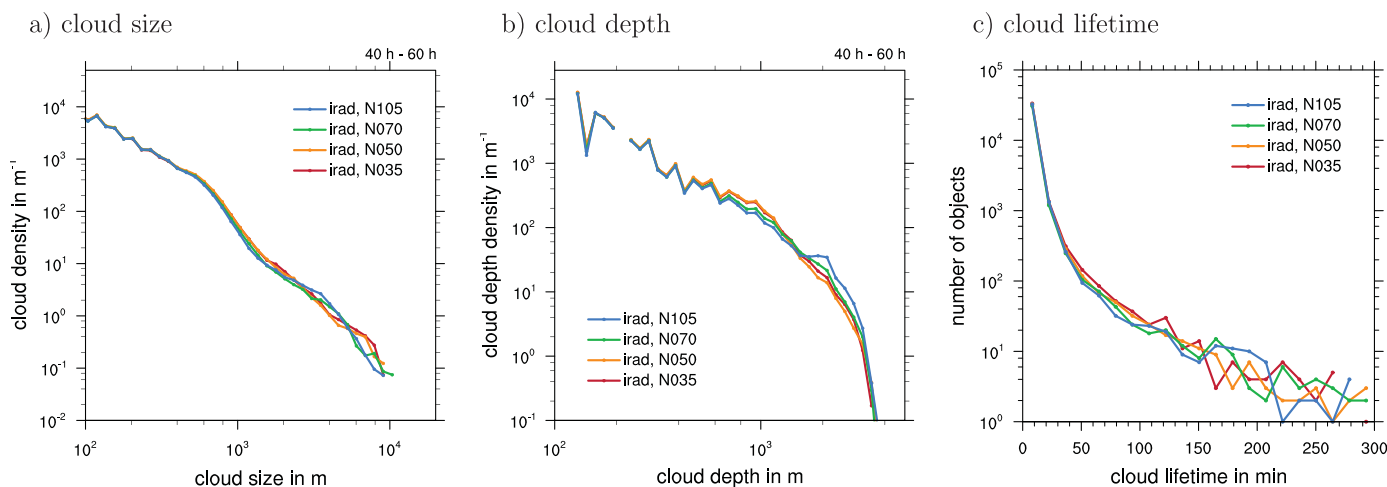
Figure 11. Results from cloud tracking for the last 20 h of the *irad-cool* simulations using the cloud identification and tracking algorithm of *Heus and Seifert* [2013].

the decomposition of the cloud clusters. The cloud (horizontal) size distribution shows no significant change with N, consistent with the response to N being primarily in the vertical growth of the clouds.

The cloud depth distribution also follows a power law through the depth of the trade inversion. With higher N, there is evidence of a reduction of cloud depths between 500 and 1500 m and an increase of cloud depth between 1500 and 2500 m, consistent with the deepening of the cloud layer and the histograms of cloud-top heights, e.g., Figure 7.

The distribution of cloud lifetimes follows roughly a double-exponential distribution with many short-lived clouds, and an exponential tail of long-lived clouds [*Sakradzija et al.*, 2015]. For cloud lifetimes exceeding 2 h, the statistics show no significant dependence on N. At shorter times (between roughly 1 and 2 h), there is evidence for a reduction of lifetimes for higher N. This implies that the cloud macrophysical changes identified in section 7 are indeed lifetime effects. Why might cloud lifetime decrease with N? The cloud classification within the *Heus and Seifert* [2013] tracking algorithm identifies these clouds as being dominated by the remnants of cloud clusters, or in other words, the upper level outflow of the mesocale arcs (shallow convective squall lines). This is consistent with the understanding developed in the previous sections, i.e., that the reduced relative humidity for higher N leads to more rapid evaporation and dissipation of the cloud remnants as they mix with their environment. Further analysis of the cloud tracking results also confirms that the remnants are already thinner to begin with for higher N, which supports the idea that microphysical effects like rain formation higher up in the cloud may also play a role in the shorter lifetime of the remnants.

9. Conclusions

We performed an extensive set of large-eddy simulations to try to understand the effects of cloud droplet number concentration on the evolution and structure of fair-weather cumulus over the ocean under subsiding conditions such as are observed over the trade wind regions. The simulations exhibit rich and complex behavior but the essential properties can be described by a fairly simple conceptual model.

Shallow cumulus developing in a subsiding large-scale environment approach a quasi-stationary state that can be understood as a generalization of radiative-convective equilibrium which we call subsiding radiative-convective equilibrium, or SRCE. Compared to radiative convective equilibrium with no ambient vertical velocity, the subsidence in SRCE acts to dry and warm the atmosphere, so clouds in SRCE are shallower and rain less. To establish SRCE, clouds must deepen sufficiently to produce the amount of precipitation demanded by the large-scale forcing. Small unorganized shallow clouds with low liquid water content are inefficient in producing precipitation but can destabilize the environment and promote the growth of deeper clouds including cumulus congestus. This deeper cloud mode often forms in clusters and readily supports the requisite rain rates of order 1 mm d^{-1}.
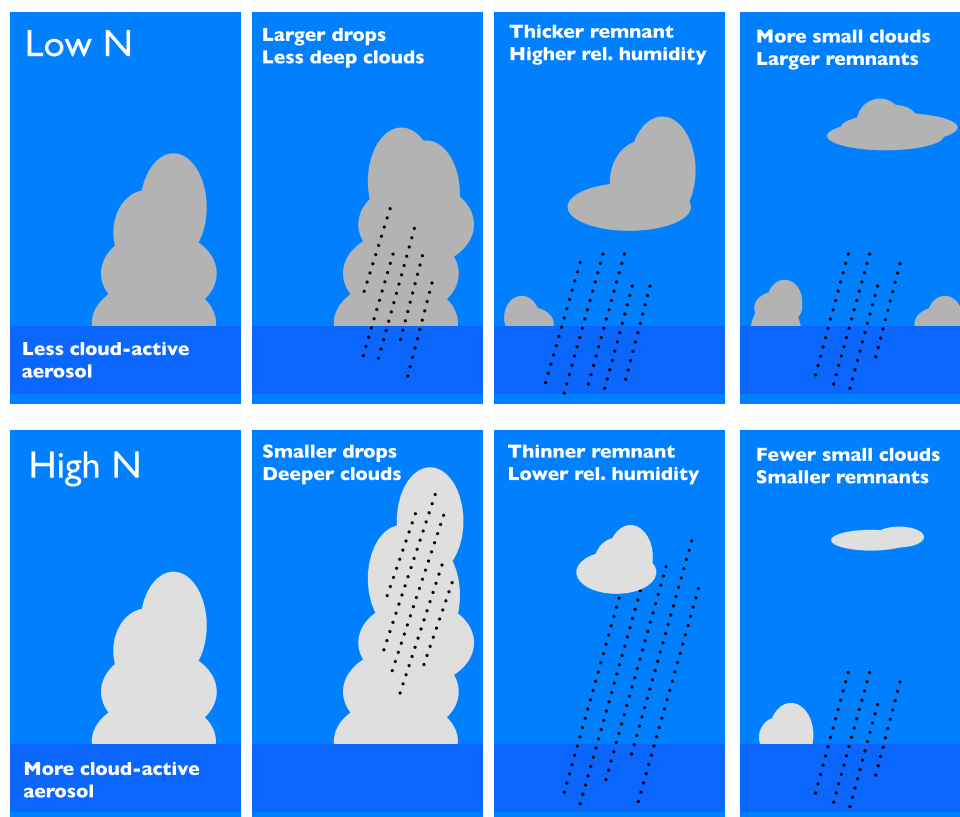
Figure 12. Conceptual model summarizing aerosol-cloud effects in the precipitating trade wind cumulus regime. Much of the response can already be understood by the deepening of the cloud layer for the high aerosol load (high N) compared to the lower aerosol conditions (low N). This comes with a lower relative humidity RH in the cloud layer. The reduced RH explains the thinner remnants which also live shorter. The lower RH is responsible for a reduction in cloud fraction just above cloud base. This negative cloud cover effect can compensate most of the increase in albedo due to brighter clouds.

Both the timescale required for the establishment of SRCE and the macrophysical distribution of clouds in the system at equilibrium depend on the microphysical properties imposed, for example, by the ambient aerosol. Rain formation is suppressed with increasing values of droplet number density N so deeper clouds must develop to produce the same rain rate as compared to low N conditions. Deeper clouds require deeper cloud layers which take longer to grow, which is why the equilibration timescale depends on N. This dependence is strong when radiative cooling rates are prescribed independent of the state of atmosphere. In more realistic simulations, radiative cooling is enhanced at the top of the cloud layer due to clear-sky cooling from water vapor. This leads to greater destabilization that accelerates the pace of equilibration and the dependence of the timescale on N is lost.

Given sufficient time, the deepening of the cloud layer efficiently buffers the effect of N on precipitation and all simulations in the quasi-stationary state develop comparable area-averaged rain rates. The shallow clouds that comprise the bulk of the cloud distribution are unaffected by changes in N; it is rather a relatively small population of deeper precipitating clouds that deepen the cloud layer and produce precipitation, and which are sensitive to microphysical state. The horizontal dimensions of these deep clouds neither depend on N nor do they contribute significantly to a change in area-averaged albedo.

An important dynamical effect of an increase in N is a reduction in relative humidity throughout the cloud and subcloud layer. This can be anticipated from the bulk budgets of SRCE because the deepening of the cloud layer associated with reduced precipitation distributes available moisture through a larger volume. Relationships between precipitation and the thermodynamic structure of the boundary layer and cloud layer have been understood with much simpler models for decades, e.g., *Albrecht* [1993] finds that the cloud layer structure is warmer, drier, and more stable with than without precipitation.

The reduced relative humidity drives the bulk of aerosol-cloud-radiation interactions. In the drier atmospheres associated with high N, the evaporation of small clouds and passive cloud remnants (the outflow of the precipitating clouds) is accelerated. This leads to a reduction in cloud cover and constitutes a negative lifetime effect, i.e., lower albedo for higher N. This leaves us with to the counterintuitive result that in precipitating trade wind cumulus regimes the total radiative effect associated with aerosol-cloud interactions may be smaller than the *Twomey* effect. In our simulations we find that cloud macroscopic changes (reductions in cloud cover) to a large extent compensate changes in cloud albedo associated with microphysical changes, i.e., the Twomey effect, so that the net effect of aerosol-cloud interactions is small and statistically indistinguishable from zero. A conceptual model of the mechanisms involved is presented schematically by Figure 12. Even this small signal may be exaggerated. We speculate further that microphysical effects may contribute to the faster evaporation of the remnants, because for high N rain forms higher up in the cloud and therefore smaller and thinner remnants are left behind. Through the use of a saturation adjustment scheme to represent the cloud droplet mode, we have neglect the dependency of cloud evaporation on cloud droplet size. Including such an effect would likely further increase the negative lifetime effect.

Some of the response of the near-equilibrium state of the system to N changes as revealed by the simulations should be observable, most prominently the deepening of the cloud layer for higher N. The conceptual model therefore provides hypotheses that might be tested observationally, e.g., by an appropriately designed field experiment. Direct observation of the aerosol-albedo effect might be much more challenging. Given the degree of dynamic and thermodynamic compensation, or buffering, on the response of cloud albedo to a change in aerosol concentrations we suspect that it may be difficult to observe and disentangle such effects in nature.

Our simulations suggest that parameterizations of cloud-aerosol effects in large-scale models are almost certain to overstate the impact of aerosols on cloud albedo and rain rate. The process understanding on which the parameterizations are based is applicable to isolated clouds in constant environments, but necessarily neglects interactions between clouds, precipitation, and circulations that, as we have shown, tend to buffer much of the impact of aerosol change. This means that the links between cloud droplet number, precipitation rate, and cloud amount are artificially direct in such models.

From a theoretical or modeling point of view, if it might be possible to reduce the uncertainty in numerical studies by performing more, longer, and bigger simulations with more accurate models, with the hope of at least being able to determine the sign of aerosol-cloud interactions, but the likely small amplitude of the effect and relative stasis in the emissions of major aerosol precursors suggest that such a study may be of purely academic interest.

Appendix A: Derivation of the Bulk Budget Equation of Subsiding Radiative-Convective Equilibrium (SRCE)

We start from a simplified large-scale moisture budget which satisfies:

$$\frac{\partial \bar{q}_t}{\partial t} + W\frac{\partial \bar{q}_t}{\partial z} + A = -\frac{\partial \overline{w'q'_t}}{\partial z} - \frac{\partial R}{\partial z} \tag{A1}$$

where an overbar denotes horizontal or Reynolds averaging, and primes denote eddy fluctuations. A large-scale advective moistening term is denoted by A and the precipitation flux by R. The large-scale velocity, W, is a prescribed subsidence velocity that is defined as the integral of a horizontal divergence, D, which we assume as constant, i.e., $W = -Dz$. The latter is a simplification over the RICO setup in which the subsidence is confined to layers below a certain depth $z_W = 2260$ m. It proves convenient to write the advective moisture source in terms of W by defining a fictitious moisture profile, q_A, such that:

$$\frac{\partial q_A}{\partial z} = -\frac{A}{W}. \tag{A2}$$

Here and in the RICO setup, we assume that both A and W are time-invariant, which means that q_A is only a function of z. Above some height z_+, which is chosen to be above the cloud layer, the large-scale moistening is prescribed to exactly balance the subsidence drying, so that $q_A(z) = q(z, t=0)$ for $z \geq z_+$.

Integrating equation (A1) from the surface to z_+, so that $\bar{q}_t - q_A = 0$ and both $\overline{w'q'_t}$ and R vanish, yields an equation for the time evolution of the integrated total water, Q, in that layer:

$$\frac{dQ}{dt} = \int_0^{z_+} \frac{\partial \bar{q}_t}{\partial t} dz = -\int_0^{z_+} W \frac{\partial}{\partial z}(\bar{q}_t - q_A) dz - \int_0^{z_+} \left(\frac{\partial \overline{w'q'_t}}{\partial z} - \frac{\partial R}{\partial z} \right) dz \tag{A3}$$

or

$$\frac{dQ}{dt} = -D(Q - Q_A) + \overline{w'q'_t}|_{\text{sfc}} - R_{\text{sfc}} \tag{A4}$$

where Q_A is the total water path corresponding to the profile $q_A(z)$. By writing, the surface flux in terms of the bulk formulae similar to equation (3),

$$\overline{w'q'_t}|_{\text{sfc}} = -C_q u_\perp (q_\perp - q_{\text{SST}}) \tag{A5}$$

with a transfer coefficient C_q and the near-surface wind speed $u_\perp$ and humidity $q_\perp$. The terms that do not depend on the evolution of the moisture profile can be grouped together into what we call the prescribed moistening:

$$M = C_q u_\perp q_{\text{SST}} + D Q_A. \tag{A6}$$

The contribution to the surface flux that depends on the near-surface humidity can be encapsulated by a parameter

$$\gamma = \frac{\bar{q}_\perp}{Q} \frac{C_q}{D} \tag{A7}$$

where γ is a dimensionless number that depends on the moisture profile. With this, we arrive at the simplified moisture budget

$$\frac{dQ}{dt} = M - DQ(1 + \gamma) - R_{\text{sfc}} \tag{A8}$$

and in case of stationarity this yields equation (2) for the equilibrium rain rate

$$R_{\text{eq}} = M - DQ(1 + \gamma). \tag{A9}$$

References

Ackerman, A. S., et al. (2009), Large-eddy simulations of a drizzling, stratocumulus-topped marine boundary layer, *Mon. Weather Rev.*, *137*(3), 1083–1110.

Albrecht, B. A. (1989), Aerosols, cloud microphysics, and fractional cloudiness, *Science*, *245*, 1227–1230.

Albrecht, B. A. (1993), Effects of precipitation on the thermodynamic structure of the trade wind boundary layer, *J. Geophys. Res.*, *98*(D4), 7327–7337, doi:10.1029/93JD00027.

Blossey, P. N., C. S. Bretherton, M. Zhang, A. Cheng, S. Endo, T. Heus, Y. Liu, A. P. Lock, S. R. de Roode, and K.-M. Xu (2013), Marine low cloud sensitivity to an idealized climate change: The cgils les intercomparison, *J. Adv. Model. Earth Syst.*, *5*, 234–258, doi:10.1002/jame.20025.

Boucher, O., et al. (2013), Clouds and aerosols, in *Climate Change 2013: The Physical Science Basis. Contribution of Working Group I to the Fifth Assessment Report of the Intergovernmental Panel on Climate Change*, edited by T. Stocker, et al., Cambridge Univ. Press, Cambridge, U. K.

Bretherton, C. S., P. N. Blossey, and C. R. Jones (2013), Mechanisms of marine low cloud sensitivity to idealized climate perturbations: A single-LES exploration extending the CGILS cases, *J. Adv. Model. Earth Syst.*, *5*, 316–337, doi:10.1002/jame.20019.

Cahalan, R. F., W. Ridgway, W. J. Wiscombe, T. L. Bell, and J. B. Snider (1994), The Albedo of Fractal Stratocumulus Clouds, *J. Atmos. Sci.*, *51*(16), 2434–2455.

Chen, Y. C., M. W. Christensen, L. Xue, A. Sorooshian, G. L. Stephens, R. M. Rasmussen, and J. H. Seinfeld (2012), Occurrence of lower cloud albedo in ship tracks, *Atmos. Chem. Phys.*, *12*(17), 8223–8235.

Christensen, M. W., and G. L. Stephens (2011), Microphysical and macrophysical responses of marine stratocumulus polluted by underlying ships: Evidence of cloud deepening, *J. Geophys. Res.*, *116*, D03201, doi:10.1029/2010JD014638.

Colon-Robles, M., R. M. Rauber, and J. B. Jensen (2006), Influence of low-level wind speed on droplet spectra near cloud base in trade wind cumulus, *Geophys. Res. Lett.*, *33*, L20814, doi:10.1029/2006GL027487.

Conover, J. H. (1969), New observations of anomalous cloud lines, *J. Atmos. Sci.*, *26*, 1153–1154.

Dawe, J. T., and P. H. Austin (2012), Statistical analysis of an les shallow cumulus cloud ensemble using a cloud tracking algorithm, *J. Atmos. Sci.*, *12*, 1101–1119.

Durkee, P. A., K. J. Noone, and R. T. Bluth (2000), The Monterey Area Ship Track Experiment, *J. Atmos. Sci.*, *57*, 2523–2541.

Feingold, G., W. R. Cotton, B. Stevens, and A. S. Frisch (1996), The Relationship between drop in-cloud residence time and drizzle production in numerically simulated stratocumulus clouds, *J. Atmos. Sci.*, *53*(8), 1108–1122.

Fu, Q., and K. N. Liou (1992), On the correlated *k*-distribution method for radiative transfer in nonhomogeneous atmospheres, *J. Atmos. Sci.*, *49*, 2139–2156.

Gerber, H. E., G. M. Frick, J. B. Jensen, and J. G. Hudson (2008), Entrainment, mixing, and microphysics in trade-wind cumulus, *J. Meteorol. Soc. Jpn.*, *86*, 87–106.

Heus, T., and A. Seifert (2013), Automated tracking of shallow cumulus clouds in large domain, long duration large eddy simulations, *Geosci. Model Dev.*, *6*, 1261–1273.

Hobbs, P., et al. (2000), Emissions from ships with respect to their effects on clouds, *J. Atmos. Sci.*, *57*(16), 2570–2590.

Hudson, J. G., and S. Noble (2014), Low-altitude summer/winter microphysics, dynamics, and CCN spectra of northeastern Caribbean small cumuli, and comparisons with stratus, *J. Geophys. Res. Atmos.*, *119*, 5445–5463, doi:10.1002/2013JD021442.

Lee, S.-S., G. Feingold, and P. Y. Chuang (2012), Effect of aerosol on cloud environment interactions in trade cumulus, *J. Atmos. Sci.*, *69*, 3607–3632.

LeMone, M. A., and E. J. Zipser (1980), Cumulonimbus vertical velocity events in GATE. Part I: Diameter, intensity and mass flux, *J. Atmos. Sci.*, *37*(11), 2444–2457.

Malkus, J., and H. Riehl (1964), Cloud structure and distributions over the tropical pacific ocean, *Tellus*, *16*(3), 275–287.

Mayer, B. (2009), Radiative transfer in the cloudy atmosphere, *Eur. Phys. J. Conf.*, *1*, 78–99.

Nair, U., R. Weger, K. Kuo, and R. Welch (1998), Clustering, randomness, and regularity in cloud fields: 5. The nature of regular cumulus cloud fields, *J. Geophys. Res.*, *103*(D10), 11,363–11,380, doi:10.1029/98JD00088.

Neggers, R., H. Jonker, and A. Siebesma (2003), Size statistics of cumulus cloud populations in large-eddy simulations, *J. Atmos. Sci.*, *60*(8), 1060–1074.

Nuijens, L., I. Serikov, L. Hirsch, K. Lonitz, and B. Stevens (2014), The distribution and variability of low-level cloud in the north Atlantic trades, *Q. J. R. Meteorol. Soc.*, *140*(684), 2364–2374, doi:10.1002/qj.2307.

Pincus, R., and B. Stevens (2009), Monte Carlo spectral integration: A consistent approximation for radiative transfer in large eddy simulations, *J. Adv. Model. Earth Syst.*, *1*, doi:10.3894/JAMES.2009.1.1.

Popke, D., B. Stevens, and A. Voigt (2013), Climate and climate change in a radiative-convective equilibrium version of ECHAM6, *J. Adv. Model. Earth Syst.*, *5*, 1–14, doi:10.1029/2012MS000191.

Ramanathan, V., and J. A. Coakley (1978), Climate modeling through radiative-convective models, *Rev. Geophys.*, *16*(4), 465–489, doi:10.1029/RG016i004p00465.

Rauber, R. M., et al. (2007), Rain in shallow cumulus over the ocean: The RICO campaign, *Bull. Am. Meteorol. Soc.*, *88*, 1912–1928.

Sakradzija, M., A. Seifert, and T. Heus (2015), Fluctuations in a quasi-stationary shallow cumulus cloud ensemble, *Nonlin. Process. Geophys.*, *22*, 65–85, doi:10.5194/npg-22-65-2015.

Saleeby, S. M., S. R. Herbener, S. C. van den Heever, and T. L'Ecuyer (2015), Impacts of cloud droplet-nucleating aerosols on shallow tropical convection, *J. Atmos. Sci.*, *72*, 1369–1385.

Seifert, A., and K. D. Beheng (2001), A double-moment parameterization for simulating autoconversion, accretion and selfcollection, *Atmos. Res.*, *59-60*, 265–281.

Seifert, A., and T. Heus (2013), Large-eddy simulation of organized precipitating trade wind cumulus clouds, *Atmos. Chem. Phys.*, *13*, 5631–5645.

Small, J. D., P. Y. Chuang, G. Feingold, and H. Jiang (2009), Can aerosol decrease cloud lifetime?, *Geophys. Res. Lett.*, *36*, L16806, doi:10.1029/2009GL038888.

Stevens, B. (2007), On the growth of layers of non-precipitating cumulus convection, *J. Atmos. Sci.*, *64*, 2916–2931.

Stevens, B. (2015), Rethinking the lower bound on aerosol radiative forcing, *J. Clim.*, *28*, 4794–4819, doi:10.1175/JCLI-D-14-00656.1.

Stevens, B., and G. Feingold (2009), Untangling aerosol effects on clouds and precipitation in a buffered system, *Nature*, *461*, 607–613.

Stevens, B., and A. Seifert (2008), Understanding macrophysical outcomes of microphysical choices in simluations of shallow cumulus convection, *J. Meteorol. Soc. Jpn.*, *86*, 143–162.

Stevens, B., C. Moeng, and P. Sullivan (1999), Large-eddy simulations-of radiatively driven convection: Sensitivities to the representation of small scales, *J. Atmos. Sci.*, *56*(23), 3963–3984.

Stevens, B., et al. (2005), Evaluation of large-eddy simulations via observations of nocturnal marine stratocumulus, *Mon. Weather Rev.*, *133*, 1443–1462.

Trivej, P., and B. Stevens (2010), The echo size distribution of precipitating shallow cumuli, *J. Atmos. Sci.*, *67*(3), 788–804.

Twomey, S. (1977), Influence of pollution on shortwave albedo of clouds, *J. Atmos. Sci.*, *34*, 1149–1152.

van Zanten, M., et al. (2011), Controls on precipitation and cloudiness in simulations of trade-wind cumulus as observed during RICO, *J. Adv. Model. Earth Syst.*, *3*, M06001, doi:10.1029/2011MS000056.

Xue, H., and G. Feingold (2006), Large-eddy simulations of trade wind cumuli: Investigation of aerosol indirect effects, *J. Atmos. Sci.*, *63*, 1605–1622.

Xue, H., G. Feingold, and B. Stevens (2008), Aerosol effects on clouds, precipitation, and the organization of shallow cumulus convection, *J. Atmos. Sci.*, *65*(2), 392–406.

Yuan, T., L. A. Remer, and H. Yu (2011), Microphysical, macrophysical and radiative signatures of volcanic aerosols in trade wind cumulus observed by the A-Train, *Atmos. Chem. Phys.*, *11*, 7119–7132.

Zhang, Y., B. Stevens, and M. Ghil (2005), On the diurnal cycle and susceptibility to aerosol concentration in a stratocumulus-topped mixed layer, *Q. J. R. Meteorol. Soc.*, *131*, 1567–1583.